Detecting the cosmological recombination signal from space

Vincent Desjacques,[1]⋆ Jens Chluba,[2,3] Joseph Silk,[3,4,5] Francesco de Bernardis[6] and Olivier Doré[7,8]

[1]*Département de Physique Théorique and Center for Astroparticle Physics (CAP), University of Geneva, 24 quai Ernest Ansermet, CH-1211 Geneva, Switzerland*
[2]*Kavli Institute for Cosmology Cambridge, Madingley Road, Cambridge CB3 0HA, UK*
[3]*Department of Physics and Astronomy, Johns Hopkins University, Baltimore, MD 21218, USA*
[4]*CNRS & UPMC, UMR 7095, Institut dAstrophysique de Paris, F-75014 Paris, France*
[5]*Laboratoire AIM-Paris-Saclay, CEA/DSM/IRFU, CNRS, Universite Paris Diderot, F-91191 Gif-sur-Yvette, France*
[6]*Department of Physics, Cornell University, Ithaca, NY 14853, USA*
[7]*Jet Propulsion Laboratory, California Institute of Technology, Pasadena, CA 91109, USA*
[8]*California Institute of Technology, Pasadena, CA 91125, USA*

ABSTRACT

Spectral distortions of the cosmic microwave background (CMB) have recently experienced an increased interest. One of the inevitable distortion signals of our cosmological concordance model is created by the cosmological recombination process, just a little before photons last scatter at redshift $z \simeq 1100$. These cosmological recombination lines, emitted by the hydrogen and helium plasma, should still be observable as tiny deviation from the CMB blackbody spectrum in the cm–dm spectral bands. In this paper, we present a forecast for the detectability of the recombination signal with future satellite experiments. We argue that serious consideration for future CMB experiments in space should be given to probing spectral distortions and, in particular, the recombination line signals. The cosmological recombination radiation not only allows determination of standard cosmological parameters, but also provides a direct observational confirmation for one of the key ingredients of our cosmological model: the cosmological recombination history. We show that, with present technology, such experiments are futuristic but feasible. The potential rewards won by opening this new window to the very early universe could be considerable.

Key words: cosmology: theory – early Universe.

1 INTRODUCTION

The cosmic microwave background (CMB) provides one of the cleanest sources of information about the Universe in which we live. In particular, the CMB temperature and polarization anisotropies have allowed us to pin down the key cosmological parameters with unprecedented precision (Bennett et al. 2003; Planck Collaboration XVI 2014a), and we are presently witnessing the final stages in the analysis of *Planck* data (Planck Collaboration XIII 2015b). Most of today's experimental effort is going into a detection of primordial *B*-modes, exploiting the curl polarization patterns sourced by gravity waves created during inflation (Kamionkowski, Kosowsky & Stebbins 1997; Seljak & Zaldarriaga 1997; Kamionkowski & Kosowsky 1998). Many balloon or ground-based experiments, such as SPIDER, BICEP2, Keck Array, Simons Array, CLASS, etc. (e.g. Crill et al. 2008; Eimer et al. 2012; Staniszewski et al. 2012; BICEP2 Collaboration et al. 2014), are currently observing or com-

ing online. These measurements will eventually exhaust all the information about the primordial Universe to be gained from the CMB anisotropies.

The next frontier in CMB measurements is the detection of spectral distortions (Silk & Chluba 2014) generated by early-energy release (Zeldovich & Sunyaev 1969; Sunyaev & Zeldovich 1970b; Illarionov & Sunyaev 1975; Danese & de Zotti 1982; Burigana, Danese & de Zotti 1991; Hu & Silk 1993; Burigana & Salvaterra 2003; Chluba & Sunyaev 2012). This is an experimental field that has not changed since *COBE*/FIRAS set upper limits on the μ and y parameters more than 20 yr ago (Fixsen et al. 1996). In the standard cosmological model, chemical potential distortions (Sunyaev & Zeldovich 1970b) are expected at a level of about 10^{-4} of the FIRAS upper limits i.e. $\mu \simeq 10^{-8}$ as a consequence of the damping of primordial adiabatic density fluctuations (Sunyaev & Zeldovich 1970c; Daly 1991; Hu, Scott & Silk 1994b; Chluba, Khatri & Sunyaev 2012a; Pajer & Zaldarriaga 2013). A detection of this signal would probe the redshift range between thermalization ($z \simeq 2 \times 10^6$) and recombination ($z \simeq 10^3$). While very interesting constraints could be derived for non-standard inflation scenarios

⋆ E-mail: Vincent.Desjacques@unige.ch

(Chluba, Erickcek & Ben-Dayan 2012b; Powell 2012; Khatri & Sunyaev 2013; Chluba & Jeong 2014; Clesse, Garbrecht & Zhu 2014), since the distortion is caused by an integrated effect of energy injection in the early Universe, it would be challenging to distinguish a detection from more exotic sources of energy, such as damping of small-scale non-Gaussian density (Ganc & Komatsu 2012; Pajer & Zaldarriaga 2012; Emami et al. 2015) or blue-tilted primordial density fluctuations (Hu & Sugiyama 1994; Dent, Easson & Tashiro 2012; Chluba & Grin 2013), or even dark matter self-annihilation (McDonald, Scherrer & Walker 2001; Chluba 2013b; Chluba & Jeong 2014).

A truly powerful probe of spectral distortions must carry redshift information. While the hybrid distortion (Chluba & Sunyaev 2012; Khatri & Sunyaev 2012; Chluba 2013a) is limited to a narrow redshift range ($10^4 \lesssim z \lesssim 3 \times 10^5$), a far more powerful probe, capable of probing the Universe directly at unprecedentedly high redshift, would be the hydrogen and helium recombination line spectrum (Dubrovich 1975; Rybicki & dell'Antonio 1993; Dubrovich & Stolyarov 1995, 1997; Sunyaev & Chluba 2009). This would be the jewel in the crown of any future spectral distortion experiment, capable of verifying the recombination history of the Universe and measuring the primordial helium fraction (e.g. Chluba & Sunyaev 2008; Sunyaev & Chluba 2009). It would simultaneously provide a unique calibration template for probing the origin of other signals such as an average y distortion (Zeldovich & Sunyaev 1969) caused by reionization and structure formation (Hu et al. 1994a; Cen & Ostriker 1999; Refregier et al. 2000) or the aforementioned dissipation signal. A cosmic recombination line probe would require extensive frequency coverage over GHz to THz frequencies and exquisite sensitivity. It would open a new window on the Universe 380 000 yr after the big bang (Sunyaev & Chluba 2009).

Here, we explore the feasibility of such a probe for a future space experiment. We will consider the following situation: low- and high-frequency channels are used to remove synchrotron radiation and thermal dust emission, respectively. At the remaining available frequencies, we can use a template for the recombination spectrum and cross-correlate it with the data. This matched-filtering approach is particularly well suited for our purpose as we are mainly interested in the detection level of the recombination spectrum. It will naturally take into account frequency correlations in the template. At the Fisher matrix level, this is equivalent to a forecast for the overall amplitude of the recombination spectrum template.

The paper is organized as follows. We begin with a description of our model for the sky signal in Section 2, with particular emphasis on the cosmic infrared background (CIB). We discuss experimental setups and present forecasts in Section 3. We conclude in Section 4. We adopt a concordance, flat Λ cold dark matter model in all illustrative calculations.

2 MODELLING THE RESIDUAL INTENSITY

We are interested in modelling the specific intensity (or brightness), $I_{res}(\nu)$, that remains after the subtraction of the average CMB blackbody spectrum as a function of frequency. Assuming that foregrounds such as dust etc. have been subtracted, this residual intensity is a sum of CMB spectral distortions, the CIB and noise induced by the incident radiation and the detector. We will now describe each of these components in more detail.

2.1 Spectral distortions of the CMB

Upon subtracting the estimated CMB monopole, we are left with primordial μ and y distortions, a temperature shift, which arises

from our imperfect knowledge of the CMB temperature, and the cosmological recombination radiation. We shall neglect the residual (non-μ/non-y or r-type) distortion signal related to the precise time-dependence of the energy release process (Chluba & Sunyaev 2012; Khatri & Sunyaev 2012; Chluba 2013a), which can add extra low intensity features to the broad primordial distortion (Khatri & Sunyaev 2012; Chluba & Jeong 2014).

For the signals, we use the definitions commonly adopted in the treatment of CMB spectral distortions (e.g. Chluba & Sunyaev 2012; Chluba et al. 2012a). For the μ distortion, a small amount of energy ΔE is injected at constant photon number into a blackbody of reference temperature T_0. Once ΔE is fully Comptonized, we are left with a Bose–Einstein spectrum with chemical potential μ (Sunyaev & Zeldovich 1970b). The intensity difference is

$$
\begin{aligned}
I^\mu(\nu) &= \mu \left(\frac{2h\nu^3}{c^2} \right) M(x) \\
&= \mu \left(\frac{2h\nu^3}{c^2} \right) G(x) \left(\frac{\pi^2}{18\zeta(3)} - \frac{1}{x} \right) .
\end{aligned} \tag{1}
$$

Here, $x = h\nu/k_B T_0$, k_B and h are the Boltzmann and Planck constants, and $G(x) = xe^x/(e^x - 1)^2$ describes a pure temperature shift. Note also that $\pi^2/[18\zeta(3)] \approx 0.4561$. The y distortion is generated by inefficient diffusion of the photons in energy through scattering off of electrons (Zeldovich & Sunyaev 1969). The change in intensity reads

$$
\begin{aligned}
I^y(\nu) &= y \left(\frac{2h\nu^3}{c^2} \right) Y(x) \\
&= y \left(\frac{2h\nu^3}{c^2} \right) G(x) \left[x \left(\frac{e^x + 1}{e^x - 1} \right) - 4 \right] .
\end{aligned} \tag{2}
$$

We must furthermore take into account the uncertainty in the temperature $T_0 = 2.726$ K (Fixsen et al. 1996; Fixsen 2009) of the reference blackbody up to second order (Chluba & Jeong 2014). At this order, the deviation from the reference blackbody intensity is the sum of a pure temperature shift and a y distortion (Zeldovich, Illarionov & Sunyaev 1972; Chluba & Sunyaev 2004; Stebbins 2007),

$$
I^T(\nu) = \frac{2h\nu^3}{c^2} \left[G(x)\Delta(1 + \Delta) + Y(x)\frac{\Delta^2}{2} \right] . \tag{3}
$$

Hence, a relative error of $\Delta = 5 \times 10^{-4} \equiv \Delta T_0/T_0$ in the precise value of T_0 generates a y distortion of amplitude $y \simeq 10^{-7}$. Patch-to-patch fluctuations in the CMB temperature will also contribute an average temperature shift (Chluba & Sunyaev 2004; Chluba et al. 2012a), which can simply be absorbed into the variable Δ.

The recombination spectrum, $I^{rec}(\nu)$, can be evaluated numerically with high accuracy. Since we are only interested in a detection of the recombination spectrum, we will use the template obtained from the computation of[1] Rubiño-Martín, Chluba & Sunyaev (2006, 2008), Chluba & Sunyaev 2006 and Chluba, Rubiño-Martín & Sunyaev (2007). These calculations include the contributions from both hydrogen and helium. Refinements caused by helium feedback processes (Chluba & Sunyaev 2010) are omitted here, but should not affect the main conclusions of this work. Similarly, small changes in recombination radiation at low frequencies ($\nu \lesssim 1$ GHz) caused by recombinations to highly excited states (Chluba, Vasil & Dursi 2010; Ali-Haïmoud 2013) are omitted.

---

[1] The data is available at http://vivaldi.ll.iac.es/galeria/jalberto/recomb/

2.2 Halo model of the CIB

Our model of the CIB is based on a halo model description of the relation between star-forming galaxies and dark matter (sub)haloes (Shang et al. 2012), which builds on the early works of Knox et al. 2001 and (Amblard & Cooray 2007, see also De Bernardis & Cooray 2012 for a model based on conditional luminosity functions).

The average CIB brightness at a given frequency (in unit of Jy sr^{-1}) is

$$I^{\text{CIB}}(\nu) = \int_0^\infty \mathrm{d}z \left(\frac{\mathrm{d}\chi}{\mathrm{d}z}\right) a(z) \bar{j}_\nu(z) , \quad (4)$$

where $\chi(z)$ is the line-of-sight comoving distance to redshift z and

$$\bar{j}_\nu(z) = \int \mathrm{d}L \, \bar{n}(L, z) \frac{L_{(1+z)\nu}}{4\pi} \quad (5)$$

is the mean emissivity of galaxies below a certain flux limit at a frequency ν and per comoving volume. Here, $L_{(1+z)\nu}$ and $\bar{n}(L, z)$ denote the infrared galaxy luminosity (in W Hz^{-1}) and galaxy luminosity function, respectively, while $(1 + z)\nu$ designates the rest-frame frequency. Following Shang et al. 2012, we split the mean emissivity into a sum of two contributions,

$$\bar{j}_\nu(z) = \int \mathrm{d}M \frac{\mathrm{d}N}{\mathrm{d}M}(M, z) \Big[f_\nu^{\text{c}}(M, z) + f_\nu^{\text{s}}(M, z) \Big] , \quad (6)$$

where

$$f_\nu^{\text{c}}(M, z) = \frac{1}{4\pi} N_{\text{c}} L_{\text{c},(1+z)\nu}(M, z) \quad (7)$$

$$f_\nu^{\text{s}}(M, z) = \frac{1}{4\pi} \int \mathrm{d}m \frac{\mathrm{d}n}{\mathrm{d}m}(M, z) L_{\text{s},(1+z)\nu}(m, z) \quad (8)$$

are the average emissivity produced by the central and satellite galaxies of a given halo at redshift z, $\mathrm{d}N/\mathrm{d}M$ and $\mathrm{d}n/\mathrm{d}m$ are the halo and subhalo mass functions, and M and m are the parent halo and subhalo masses. The numbers N_{c} and N_{s} of central and satellite galaxies are specified by the halo occupation distribution (HOD; Berlind & Weinberg 2002; Zheng et al. 2005). The total number of galaxies in a given halo of mass M thus is $N_{\text{c}} + N_{\text{s}}$. Numerical simulations indicate that N_{c} typically follows a step-like function (Kravtsov et al. 2004), while N_{s} can be parametrized by a power law with logarithmic slope $\alpha \approx 1$. For the characteristic mass M_{cen} of the step function, we ignore any luminosity dependence and adopt a value of $3 \times 10^{11} \, \text{M}_\odot \, h^{-1}$ broadly consistent with the best-fitting HOD models of Zehavi et al. 2011. In all subsequent calculations, we use the halo and subhalo mass functions provided by Tinker et al. 2008 and Tinker & Wetzel 2010, and integrate the subhalo mass function from a minimum halo mass $M_{\text{min}} = 10^{10} \, \text{M}_\odot \, h^{-1}$ to the parent halo mass M.

We assume that the same luminosity–mass relation holds for both central and satellite galaxies, and relate the galaxy infrared luminosity to the host halo mass through the parametric relation (Shang et al. 2012),

$$L_{(1+z)\nu}(M, z) = L_0 \Phi(z) \Sigma(M) \Theta[(1 + z)\nu] , \quad (9)$$

where L_0 is an overall normalization that must be constrained from measurement of the CIB specific intensity in a given frequency range. The term $\Phi(z)$ describes the redshift-dependence of the normalization. We adopt the power-law scaling, $\Phi(z) = (1 + z)^{3.6}$, whereas, for the dependence $\Sigma(M)$ of the galaxy luminosity on halo mass, we assume a lognormal distribution with mean mass $M_{\text{eff}} = 4.43 \times 10^{12} \, \text{M}_\odot \, h^{-1}$ and variance $\sigma_{\text{M/L}}^2 = 0.5$ (as in Planck Collaboration XXX 2014b). M_{eff} characterizes the peak and $\sigma_{\text{M/L}}$
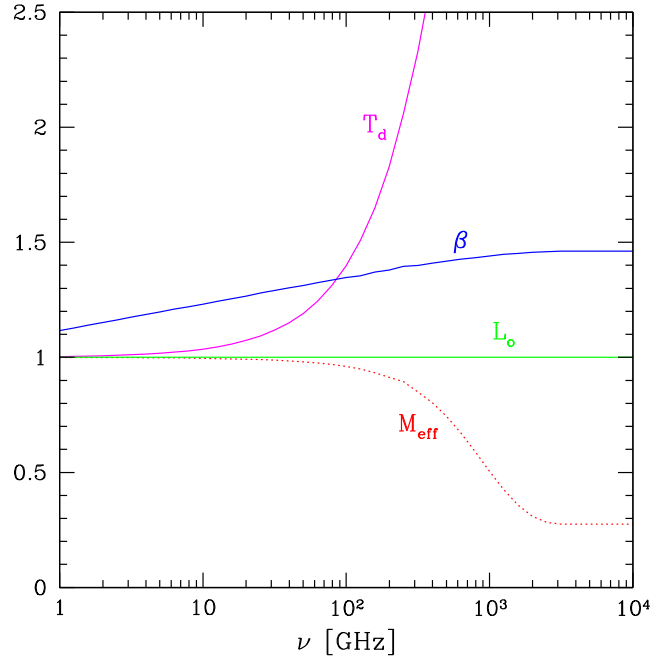

Figure 1. Logarithmic derivatives $\partial \ln I^{\text{CIB}} / \partial p_\alpha(\nu)$ of the average CIB intensity w.r.t. the model parameters $\boldsymbol{p} = (M_{\text{eff}}, T_d, \beta, L_0)$. The results are normalized such that all the derivatives are equal to unity for $\nu = 0.1$ GHz. Dotted curves indicate negative values.

the range of halo mass that produces a given luminosity L. Although our choice of $\sigma_{\text{M/L}}^2 = 0.5$ is somewhat arbitrary, the CIB angular power spectra turn out to be fairly insensitive to $\sigma_{\text{M/L}}$ (Shang et al. 2012). In addition, the value of M_{eff} is consistent with the peak of the stellar-to-halo mass ratio inferred from semi-analytic galaxy formation models (Guo et al. 2010).

For the galaxy spectral energy distribution (SED), we assume a modified blackbody shape with a power-law emissivity as in Hall et al. 2010,

$$\Theta(\nu, z) \propto \begin{cases} \nu^\beta B_\nu(T_d) & \nu \le \nu_0 \\ \nu^{-\gamma} & \nu > \nu_0 \end{cases} , \quad (10)$$

where $B_\nu(T)$ is the brightness of a blackbody with temperature T, T_d is the dust temperature and β is the dust emissivity index. The grey-body and power-law connect smoothly at ν_0 provided that

$$\left. \frac{\mathrm{d}\ln\Theta(\nu, z)}{\mathrm{d}\ln\nu} \right|_{\nu_0} = -\gamma . \quad (11)$$

In principle, T_d and β should be allowed to vary on an object-by-object basis. However, their distribution is not known. Furthermore, we integrate over a wide range of redshift and, therefore, smooth out deviations from the average spectrum. Therefore, we will assume the same T_d and β for all galaxies for simplicity. Unlike Serra et al. 2014, however, we will treat both the dust emissivity index β and the dust temperature T_d as free parameters, while we fix the SED index gamma to its mean value of $\gamma = 1.7$ found by Planck Collaboration XXX 2014b. The reason is that, at frequencies $\nu \lesssim 10^3$ GHz, a change in the value of β tilts the CIB intensity in a way that could mimic a μ/y distortion or the broad-band shape of the recombination spectrum. This is illustrated in Fig. 1, in which we show logarithmic derivatives of the average CIB intensity w.r.t. our free model parameters $(M_{\text{eff}}, T_d, \beta, L_0)$ around the fiducial value $(M_{\text{eff}}, T_d, \beta, L_0) = (4.43 \times 10^{12} \, \text{M}_\odot \, h^{-1}, 26 \, \text{K}, 1.7, 4.8 \times 10^{-40}$

W Hz^{-1}). Clearly, the logarithmic derivative $\partial \ln I^{\mathrm{CIB}} / \partial \beta$ cannot be expressed as linear combination of the other derivatives, so we must treat β as free parameter since it is not well constrained by the data. We will adopt a fiducial value of $\beta = 1.7$.

Note that the spectrum of star-forming galaxies typically features broad emission lines in mid-infrared (from 10 to 30 µm) caused mainly by polycyclic aromatic hydrocarbon (PAH) molecules (e.g. Leger & Puget 1984; Allamandola, Tielens & Barker 1985; Smith et al. 2007), but these are far on the blue side of the spectrum ($\nu \gtrsim 10^4$ GHz). By contrast, C II emission lines from high-redshift galaxies for instance contribute an additional foreground, even though we neglect them here for simplicity.

2.3 CIB anisotropies

While we will ignore fluctuations in the μ and y distortions across the sky,[2] we must take into account anisotropies in the CMB and CIB intensity. In principle, it should be possible to subtract at least partly both CMB and CIB anisotropies from the observed patch using, e.g. data from the *Planck* experiment. In our fiducial analysis, however, we will assume they have not been removed. Therefore, we must include them in the Fisher information as they will contribute to the covariance of the signal, especially if the surveyed patch is small.

The CIB intensity at a given frequency ν and in a given direction $\hat{\boldsymbol{n}}$ can be expressed as the line-of-sight integral

$$I^{\mathrm{CIB}}(\nu, \hat{\boldsymbol{n}}) = \int_0^\infty \mathrm{d}z \left(\frac{\mathrm{d}\chi}{\mathrm{d}z}\right) a(z) \bar{j}_\nu(z) \left(1 + \frac{\delta j_\nu(\chi(z)\hat{\boldsymbol{n}}, z)}{\bar{j}_\nu(z)}\right).$$

Using the Limber approximation (Limber 1954), the angular cross-power spectrum of CIB anisotropies at observed frequencies ν and ν' is (Knox et al. 2001)

$$C_\ell^{\mathrm{CIB}}(\nu, \nu') = \int_0^\infty \frac{\mathrm{d}z}{\chi^2} \left(\frac{\mathrm{d}\chi}{\mathrm{d}z}\right) a^2(z) \, \bar{j}_\nu(z) \bar{j}_{\nu'}(z)$$
$$\times P_j^{\nu \times \nu'}(k = \ell/\chi, z) \,. \tag{12}$$

Assuming that spatial variations in the emissivity trace fluctuations in the galaxy number density, i.e. $\delta j / \bar{j} = \delta n_{\mathrm{g}} / \bar{n}_{\mathrm{g}}$, the power spectrum P_j is equal to the galaxy power spectrum P_{g}. In the framework of the halo model discussed above, we thus have

$$P_j^{\nu \times \nu'}(k, z) = P_{1\mathrm{h}}^{\nu \times \nu'}(k, z) + P_{2\mathrm{h}}^{\nu \times \nu'}(k, z) + \mathrm{shot - noise} \,. \tag{13}$$

Hereafter, we will ignore the shot-noise contribution because it is typically smaller than the two-halo term on large scales. The contributions from galaxy pairs in the same halo, the so-called one-halo term, is

$$P_{1\mathrm{h}}^{\nu \times \nu'}(k, z) = \frac{1}{\bar{j}_\nu \bar{j}_{\nu'}} \int \mathrm{d}M \frac{\mathrm{d}N}{\mathrm{d}M} \Big[f_\nu^{\mathrm{c}}(M, z) f_{\nu'}^{\mathrm{s}}(M, z) u(k, z|M)$$
$$+ f_{\nu'}^{\mathrm{c}}(M, z) f_\nu^{\mathrm{s}}(M, z) u(k, z|M)$$
$$+ f_\nu^{\mathrm{s}}(M, z) f_{\nu'}^{\mathrm{s}}(M, z) u^2(k, z|M) \Big] \,, \tag{14}$$

[2] The largest fluctuations are related to the spatially varying y distortion signal caused by warm-hot intergalactic medium and unresolved clusters (e.g. Cen & Ostriker 1999; Miniati et al. 2000; Refregier et al. 2000; Zhang, Pen & Trac 2004), while significant spatially varying μ distortions can only be created by anisotropic energy release processes (Chluba et al. 2012a), for example, related to primordial non-Gaussianity (Ganc & Komatsu 2012; Pajer & Zaldarriaga 2012).

where $u(k, z|M)$ is the normalized Fourier transform of the halo density profile, whereas the two-halo term reads

$$P_{2\mathrm{h}}^{\nu \times \nu'}(k, z) = \frac{1}{\bar{j}_\nu \bar{j}_{\nu'}} D_\nu(k, z) D_{\nu'}(k, z) P_{\mathrm{lin}}(k, z) \,, \tag{15}$$

with

$$D_\nu(k, z) = \int \mathrm{d}M \frac{\mathrm{d}N}{\mathrm{d}M} b_1(M, z) u(k, z|M)$$
$$\times \left[f_\nu^{\mathrm{c}}(M, z) + f_\nu^{\mathrm{s}}(M, z) \right] \,. \tag{16}$$

Here, P_{lin} is the linear mass power spectrum extrapolated to redshift z, whereas b_1 is the (Eulerian) linear halo bias that follows from a peak-background split applied to the halo mass function $\mathrm{d}N/\mathrm{d}M$. For consistency, we use the fitting formula given in Tinker et al. 2010. The one-halo term can only be seen with high angular resolution surveys reaching out to arcminute scales.

The CIB intensity reported in each pixel of the surveyed patch can be written as

$$I^{\mathrm{CIB}}(\nu, \hat{\boldsymbol{n}}_i) = \int \mathrm{d}\hat{\boldsymbol{n}} \, I^{\mathrm{CIB}}(\nu, \hat{\boldsymbol{n}}) B(\hat{\boldsymbol{n}}, \hat{\boldsymbol{n}}_i), \tag{17}$$

where $B(\hat{\boldsymbol{n}}, \hat{\boldsymbol{n}}_i)$ is the beam profile. Specializing to azimuthally symmetric beam patterns, $B(\hat{\boldsymbol{n}}, \hat{\boldsymbol{n}}_i)$ is a function of $\hat{\boldsymbol{n}} \cdot \hat{\boldsymbol{n}}_i$ solely, and can thus be expanded in the Legendre polynomials P_ℓ,

$$B(\hat{\boldsymbol{n}} \cdot \hat{\boldsymbol{n}}_i) = \frac{1}{4\pi} \sum_{\ell=0}^\infty (2\ell + 1) B_\ell P_\ell(\hat{\boldsymbol{n}} \cdot \hat{\boldsymbol{n}}_i) \,. \tag{18}$$

While this is an approximation that is not met in most current experimental designs, it is straightforward to generalize the computation. Our main conclusions will not change. For a single Gaussian beam profile,

$$B(\hat{\boldsymbol{n}} \cdot \hat{\boldsymbol{n}}_i) = \frac{1}{2\pi\sigma_{\mathrm{B}}^2} \exp\left(-\frac{\vartheta^2}{2\sigma_{\mathrm{B}}^2}\right) \tag{19}$$

with $\hat{\boldsymbol{n}} \cdot \hat{\boldsymbol{n}}_i = \cos\vartheta$ and σ_{B} is related to the full width half-maximum (FWHM) ϑ_{B} of the beam in radians through $\vartheta_{\mathrm{B}} \approx 2.3548\sigma_{\mathrm{B}}$. In this case, the series coefficients are well approximated by (Silk & Wilson 1980; Bond & Efstathiou 1984; White & Srednicki 1995)

$$B_\ell \approx \exp\left(-\frac{1}{2}\ell(\ell+1)\sigma_{\mathrm{B}}^2\right) \,. \tag{20}$$

The CIB intensity averaged over the surveyed patch reads

$$\bar{I}^{\mathrm{CIB}}(\nu) = \frac{1}{\Omega_{\mathrm{s}}} \int_{\Omega_{\mathrm{s}}} \mathrm{d}\hat{\boldsymbol{n}}_i \int \mathrm{d}\hat{\boldsymbol{n}} \, I^{\mathrm{CIB}}(\nu, \hat{\boldsymbol{n}}) B(\hat{\boldsymbol{n}} \cdot \hat{\boldsymbol{n}}_i)$$
$$= \frac{1}{\Omega_{\mathrm{s}}} \sum_{\ell m} B_\ell \int_{\Omega_{\mathrm{s}}} \mathrm{d}\hat{\boldsymbol{n}}_i \int \mathrm{d}\hat{\boldsymbol{n}} \, I^{\mathrm{CIB}}(\nu, \hat{\boldsymbol{n}}) Y_\ell^{m\star}(\hat{\boldsymbol{n}}) Y_\ell^m(\hat{\boldsymbol{n}}_i) \,. \tag{21}$$

Here, $\Omega_{\mathrm{s}} = 4\pi f_{\mathrm{sky}}$ is the area of the surveyed patch. For an azimuthally symmetric patch centred at $\vartheta = 0$ (for simplification), the integral over the unit vector $\hat{\boldsymbol{n}}_i$ trivially is

$$\int_{\Omega_{\mathrm{s}}} \mathrm{d}\hat{\boldsymbol{n}}_i Y_l^m(\hat{\boldsymbol{n}}_i) \equiv W_l \delta_{\mathrm{m0}} \,. \tag{22}$$

For a circular cap (i.e. unit weight for all pixels with polar angle such that $\vartheta \leq \vartheta_W$), the harmonic transform W_ℓ of the survey window is (e.g. Manzotti, Hu & Benoit-Lévy 2014)

$$W_\ell = \sqrt{\frac{\pi}{2\ell + 1}} \left[P_{\ell+1}(x) - P_{\ell-1}(x) \right] \,.$$

Here, $P_\ell(x)$ denote Legendre polynomials and $x = \cos\vartheta_W = 1 - 2f_{\mathrm{sky}}$ is the cosine of the opening angle. Substituting the multipole

expansions for the survey mask and the beam profile, the partial sky average of $I^{\text{CIB}}(\nu, \hat{\boldsymbol{n}})$ simplifies to

$$\bar{I}(\nu) = \frac{1}{\Omega_{\text{s}}} \sum_{\ell} W_{\ell} B_{\ell} \int \mathrm{d}\hat{\boldsymbol{n}} \, I^{\text{CIB}}(\nu, \hat{\boldsymbol{n}}) Y_{\ell}^{0}(\hat{\boldsymbol{n}}) . \tag{23}$$

In the linear bias approximation, the Fourier modes of the CIB fluctuations are determined by $\delta j_{\nu}(\boldsymbol{k}, z) = \bar{j}_{\nu}(z) b(k, \nu, z) \delta(\boldsymbol{k}, z)$. If we now successively write $\delta j_{\nu}(\chi(z)\hat{\boldsymbol{n}}, z)$ as the Fourier transform of $\delta j_{\nu}(\boldsymbol{k}, z)$, substitute the plane–wave expansion and use the Limber approximation, then the frequency-dependent multipoles, $a_{\ell 0}(\nu)$, can eventually be written as the line-of-sight integral (Knox et al. 2001)

$$a_{\ell 0}(\nu) = \sqrt{4\pi} I^{\text{CIB}}(\nu) \delta_{\ell 0} + i^{\ell} \frac{\sqrt{\pi}}{2} \int \frac{\mathrm{d}^3 k}{2\pi^2} \frac{\Gamma((\ell+1)/2)}{\Gamma((\ell+2)/2)}$$
$$\times a(\bar{z}) D(\bar{z}) \bar{j}_{\nu}(\bar{z}) \frac{b(k, \nu, \bar{z})}{k} \delta(\boldsymbol{k}) Y_{\ell}^{0}(\hat{\boldsymbol{k}}) . \tag{24}$$

Here, $D(z)$ is the linear growth rate and $\bar{z}$ is defined through the relation $k\chi(\bar{z}) \approx \ell$. The monopole of the CIB intensity computed from patches of the sky with coverage fraction $f_{\text{sky}} = \Omega_{\text{s}}/(4\pi)$ is thus given by

$$\bar{I}(\nu) = \frac{1}{\Omega_{\text{s}}} \sum_{\ell} W_{\ell} B_{\ell} \, a_{\ell 0}(\nu), \tag{25}$$

where the multipole coefficients $a_{\ell 0}(\nu)$ are given by equation (24). Of course, the average $\langle \bar{I}^{\text{CIB}}(\nu) \rangle$ over all such patches is exactly given by $W_0 B_0 a_{00}(\nu) \equiv I^{\text{CIB}}(\nu)$. However, owing to cosmic variance, the monopole fluctuates from patch to patch with an amplitude given by

$$\left[\delta \bar{I}^{\text{CIB}}(\nu)\right]^2 = \left\langle \bar{I}^{\text{CIB}}(\nu)^2 \right\rangle - \left\langle \bar{I}^{\text{CIB}}(\nu) \right\rangle^2$$
$$= \frac{1}{\Omega_{\text{s}}^2} \sum_{\ell, \ell' \geq 1} W_{\ell} W_{\ell'}^{\star} B_{\ell} B_{\ell'}^{\star} \langle a_{\ell 0}(\nu) a_{\ell' 0}^{\star}(\nu) \rangle$$
$$= \frac{1}{\Omega_{\text{s}}^2} \sum_{\ell \geq 2} |W_{\ell} B_{\ell}|^2 C_{\ell}^{\text{CIB}}(\nu, \nu) , \tag{26}$$

where the cross-power spectrum $C_{\ell}^{\text{CIB}}(\nu, \nu)$ is given by equation (12). Note that, following Knox et al. 2001, we have used the Limber approximation and approximated the ratio of Gamma functions squared in equation (24) as $\approx 2/\ell$ to simplify the ensemble average $\langle a_{\ell 0}(\nu) a_{\ell' 0}^{\star}(\nu) \rangle$. Therefore, our result strictly holds for $\ell \gg 1$.

2.4 CMB primary and secondary anisotropies

CMB anisotropies will also contribute to the covariance of the signal if they are not taken out. Ignoring the weak frequency dependence induced by Rayleigh scattering (Takahara & Sasaki 1991; Yu, Spergel & Ostriker 2001; Lewis 2013), the residual CMB intensity (i.e. with the reference blackbody spectrum subtracted) averaged over the surveyed patch reads

$$\bar{I}^{\text{CMB}}(\nu) \approx I^T(\nu) \qquad \text{with} \qquad T \approx \Delta + \bar{\Theta} . \tag{27}$$

Here, Δ is the relative uncertainty on the temperature of the monopole and $\bar{\Theta}$ is the average temperature anisotropy in the surveyed window. In analogy with the CIB, the variance of CMB intensity fluctuations across different patches of the sky reads

$$\left[\delta \bar{I}^{\text{CMB}}(\nu)\right]^2 = \frac{1}{\Omega_{\text{s}}^2} \sum_{\ell \geq 2} |W_{\ell} B_{\ell}|^2 C_{\ell}^{\text{CMB}}(\nu, \nu) , \tag{28}$$

where the CMB intensity power spectrum is given by

$$C_{\ell}^{\text{CMB}}(\nu, \nu) \approx \left(\frac{2h\nu^3}{c^2}\right)^2 G^2(x) \, C_{\ell} . \tag{29}$$

The contribution from Thomson scattering takes on the standard expression:

$$C_{\ell} = \frac{2}{\pi} \int_0^{\infty} \mathrm{d}k \, k^2 g_{T\ell}^2(k) P_{\Phi}(k), \tag{30}$$

where $g_{T\ell}(k)$ denotes the photon transfer function, which can be obtained from CAMB (Lewis, Challinor & Lasenby 2000). We will assume that CMB intensity fluctuations are fully characterized by the primordial scalar amplitude A_{s}.

The variance of primordial μ- and y-distortions fluctuations (created before recombination) over patches can be ignored, since the current limits on the magnitude of y and μ are fairly small so that fluctuations are expected to contribute at the $\delta I_{\nu}/I_{\nu} \simeq 10^{-10}$ level. Larger fluctuations of μ and y across the sky could be created by the dissipation of acoustic modes with modulated small-scale power due to non-Gaussianity in the ultrasqueezed limit (Ganc & Komatsu 2012; Pajer & Zaldarriaga 2012), however, current upper limits on $f_{\text{NL}} \lesssim 2.5 \pm 5.7$ (Planck Collaboration XVII 2015a) suggest that this case is unlikely for scale-invariant non-Gaussianity, so that we ignore it here.

Secondary y distortions arise in the late-time Universe because CMB photons scatter off hot electrons present in the gas of filaments and galaxy clusters (Sunyaev & Zeldovich 1970a). The magnitude of this y distortion is an integral of the electron pressure along sight lines passing through the large-scale structure (LSS). In a typical cluster, the electron temperature is $T_{\text{e}} \sim 1$ keV and leads to $y \sim 10^{-6}$. Existing catalogues of galaxy clusters can be used to remove at least part of the signal generated at low redshift (i.e. large angular scales). Nevertheless, we will be left with a residual monopole, which can be absorbed into $I^{y}(\nu)$ as long as one is not interested in the primordial y distortion, and a fluctuating contribution, whose angular power spectrum is (within the Limber approximation, see Persi et al. 1995; Refregier et al. 2000)

$$C_{\ell}^{\text{SZ}}(\nu, \nu) \sim y_0^2 \left(\frac{2h\nu^3}{c^2}\right)^2 Y^2(x)$$
$$\times \int_0^{\infty} \frac{\mathrm{d}z}{\chi^2} \left(\frac{\mathrm{d}\chi}{\mathrm{d}z}\right) \frac{\bar{T}_{\rho}^2}{a^4(z)} P_{\text{p}}(k = \ell/\chi, z), \tag{31}$$

where the constant y_0 is $\sim 1.7 \times 10^{-16}$ K^{-1} Mpc^{-1} for a helium fraction and baryon density consistent with big bang nucleosynthesis constraints, $\bar{T}_{\rho}$ is the volume-average, density-weighted gas temperature and $P_p(k, z)$ is the three-dimensional power spectrum of pressure fluctuations.

For simplicity, we will assume that $P_{\text{p}}(k, z) = b_{\text{p}}^2 P_{\text{lin}}(k, z)$ is a biased version of the linear mass power spectrum. We adopt $b_{\text{p}} = 85$, which yields a prediction consistent with the simulations of Refregier et al. 2000 and, thus, provides a realistic upper limit to the signal. We compute $\bar{T}_{\rho}$ as the halo virial temperature T_{vir} weighted by the mass function,

$$\bar{T}_{\rho} = \frac{1}{\bar{\rho}_{\text{m}}} \int \mathrm{d}M \, M \frac{\mathrm{d}N}{\mathrm{d}M}(M, z) T_{\text{vir}}(M, z) , \tag{32}$$

where $\bar{\rho}_{\text{m}}$ is the present-day average matter density, and

$$T_{\text{vir}}(M, z) = 6.03 \times 10^7 \beta^{-1} \left(\frac{\Delta_{\text{vir}}(z)}{18\pi^2}\right)^{1/3} \left(\frac{M}{10^{15} \, \text{M}_{\odot} \, h^{-1}}\right)^{2/3}$$
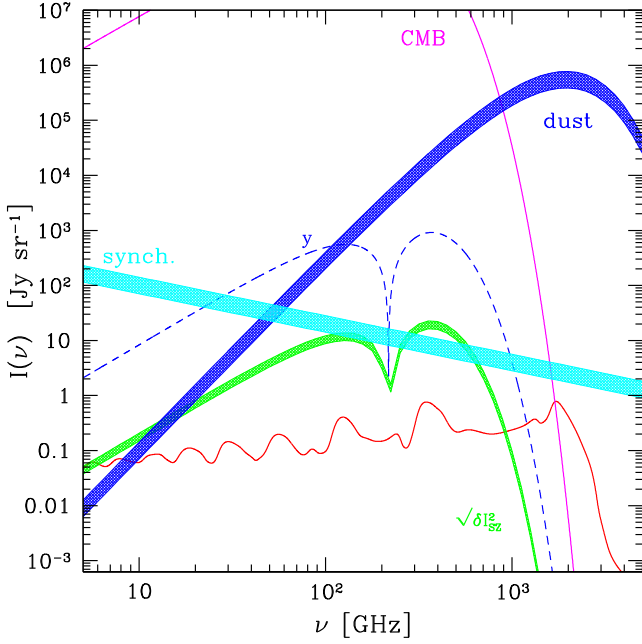$$\times (1 + z) \, \Omega_{\text{m}} \, \text{K} . \tag{33}$$

Figure 2. Contribution of galactic foregrounds and LSS-induced *y* distortions to the intensity as a function of frequency. The various curves represent the CMB monopole, galactic dust and synchrotron emission. We have also shown the monopole of the *y* distortion (primordial + LSS) with amplitude $y = 5 \times 10^{-7}$, as well as its expected rms variance (generated by LSS thermal SZ effect) for a nearly all-sky survey ($f_{sky} = 0.8$) with a beam FWHM of 1°6. The specific intensity is in unit of Jansky per unit solid angle, Jy sr^{-1}, where 1 Jy $= 10^{-26}$ W m^{-2} Hz^{-1}.

Hence, $\bar{T}_\rho$ is a strongly decreasing function of redshift. We adopt $\Delta_{vir} \equiv 200$ at all redshift to be consistent with our choice of the halo mass function, and assume $\beta = 2/3$ as in Komatsu & Kitayama 1999. Furthermore, we only include haloes in the mass range $M_{min} \leq M \leq M_{max}(z)$. While we consider a fixed minimum mass $M_{min} = 10^{10} \, M_\odot \, h^{-1}$,[3] we allow $M_{max}(z)$ to vary with redshift to account for the possibility of removing the SZ contribution from low-redshift clusters.

In Fig. 2, we show the square root of

$$\left[\delta\bar{I}^{SZ}(\nu)\right]^2 = \frac{1}{\Omega_s^2} \sum_{\ell \geq 2} |W_\ell B_\ell|^2 C_\ell^{SZ}(\nu, \nu), \tag{34}$$

for an experiment with $f_{sky} = 0.8$ and 1°6 angular resolution. The upper limit of the shaded region assumes $M_{max} = 10^{18} \, M_\odot \, h^{-1}$ at all redshifts. This corresponds to the signal that would be measured, had we not attempted to remove some of the *y* distortion using external galaxy cluster catalogues. By contrast, the lower limit of the shaded region assumes that the SZ effect from groups and clusters with $T_{vir} \geq 1$ keV has been removed, so that $M_{max}(z)$ truly depends on redshift in our calculation. Note that these two limiting cases differ by $\lesssim 50$ per cent, which shows that the contribution from virialized structures in filaments is quite substantial. Overall, for the sky coverage adopted here, fluctuations in the *y* distortions from the thermal SZ effect are of magnitude comparable to the recombination spectrum. Of course, $[\delta\bar{I}^{SZ}(\nu)]^2$ is exactly zero for an all-sky survey. For a ground-based survey targeting a 16 deg^2 patch of the sky

as discussed below (see Section 3.2), $[\delta\bar{I}^{SZ}(\nu)]^2$ is approximately 10 times larger than shown in Fig. 2.

We will hereafter ignore the signal covariance induced by the LSS through the thermal SZ effect as we will either consider satellite missions with $f_{sky} \approx 1$, or a ground-based experiment for which $[\delta\bar{I}^{CMB}(\nu)]^2$ and $[\delta\bar{I}^{CIB}(\nu)]^2$ dominate the signal covariance. Notwithstanding, one should bear in mind that the LSS *y* distortion could contribute significantly to the covariance as well as bias the primordial *y* interpretation if the sky fraction is significantly less than unity.

For comparison, we also show in Fig. 2 the average *y* distortion for $y = 5 \times 10^{-7}$, together with the approximate level of galactic emission from synchrotron and thermal dust (for which we assumed a power-law and grey-body spectrum, respectively). While we can reasonably handle the synchrotron emission with the low frequencies, removing the galactic dust monopole is more challenging as it is typically brighter than the CIB, and has a similar grey-body spectrum. Furthermore, the galactic dust emission fluctuates significantly at large angular scales ($\ell \lesssim 100$), with a power spectrum $C_\ell \propto \ell^{-2.6}$ (rather than $C_\ell \propto \ell$ for the CIB).

3 FORECAST FOR THE RECOMBINATION SPECTRUM

Our model of the total (monopole) intensity $\bar{I}_{tot}(\nu)$ measured over a patch of the sky with coverage fraction f_{sky} and in a frequency bin centred at ν_α is

$$\bar{I}^{tot}(\nu_\alpha) = I^y(\nu_\alpha) + I^\mu(\nu_\alpha) + I^T(\nu_\alpha)$$
$$+ I^{rec}(\nu_\alpha) + \bar{I}^{CIB}(\nu_\alpha) + \mathcal{N}(\nu_\alpha), \tag{35}$$

where $I^{rec}(\nu_\alpha)$ is the recombination signal which we wish to detect and the noise, $\mathcal{N}(\nu_\alpha)$, includes contribution from the incident radiation and from the detector. For simplicity, we have assumed that foreground emission within our own Galaxy from synchrotron radiation of cosmic ray electrons and thermal emission from dust grains has been separated out from the signal using low- and high-frequency channels. We leave a more detailed analysis of foreground removal (including the CIB signal) for future work.

The various signal components are shown in Fig. 3, together with the frequency coverage and sensitivity expected for the PIXIE (Kogut et al. 2011), PRISM (André et al. 2014) and MILLIMETRON (Smirnov et al. 2012) satellites, and a ground-based C II experiment (Gong et al. 2012). The dott–dashed curves represent the rms variance of CMB and CIB fluctuations in a patch of 16 deg^2 assuming a (Gaussian) beam FWHM of 0.5 arcmin. For such a small sky fraction ($f_{sky} \sim 4 \times 10^{-4}$), these are a few order of magnitudes larger than the signal in the frequency range 100–1000 GHz.

3.1 Fisher matrix

Consider N_ν uncorrelated frequency bins centred at ν_α and of bandwidth $\delta\nu$ covering the range (ν_{min}, ν_{max}). Following Tegmark, Taylor & Heavens (1997), the Fisher matrix is given by[4]

$$F_{ij} = \sum_{\alpha=1}^{N_\nu} \left[\frac{1}{2} tr\left(C_\alpha^{-1} \frac{\partial C_\alpha}{\partial p_i} C_\alpha^{-1} \frac{\partial C_\alpha}{\partial p_j} \right) + \frac{\partial \langle \boldsymbol{x}_\alpha \rangle}{\partial p_i} C_\alpha^{-1} \frac{\partial \langle \boldsymbol{x}_\alpha \rangle}{\partial p_j} \right],$$

---

[3] We have found that our predictions hardly change if we set $M_{min} = 10^{12} \, M_\odot \, h^{-1}$.

[4] Although the trace is unnecessary here because the signal is one-dimensional, we keep it for the sake of generality.
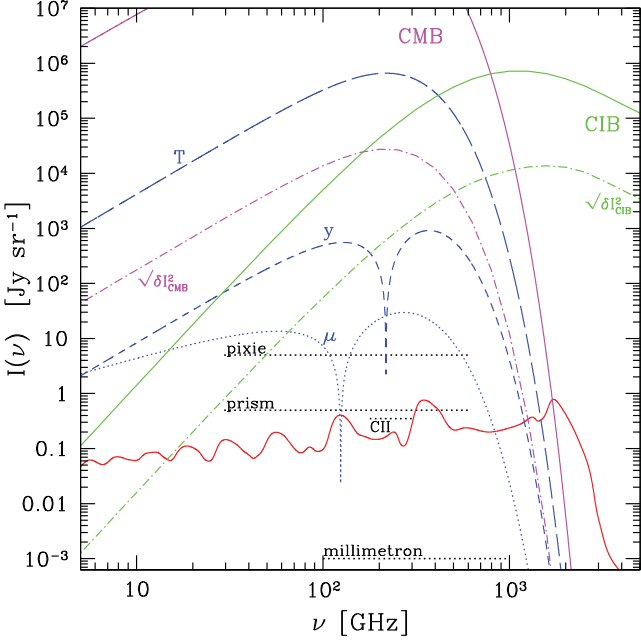
Figure 3. Average intensity as a function of frequency. The various curves represent the CMB and CIB monopole, the T, μ and y distortions and the recombination spectrum. The dott–dashed curves labelled as $\sqrt{\delta I_{\rm CMB}^2}$ and $\sqrt{\delta I_{\rm CIB}^2}$ indicate the rms variance of CMB and CIB fluctuations measured in a 16 deg^2 patch of the sky with a beam FWHM of 0.5 arcmin. The horizontal dotted lines show the frequency coverage and sensitivity expected for the PIXIE, PRISM and MILLIMETRON space experiments, as well as for a ground-based C II experiment. Note that the galactic dust monopole (not shown on this figure) is a grey-body similar to, though usually brighter than, the CIB (see Fig. 2).

where $\langle \boldsymbol{x}_\alpha \rangle = \langle \bar{I}^{\rm tot}(\nu_\alpha) \rangle$ is the ensemble average of the residual intensity over random realizations of the surveyed patch, C_α is the covariance of $I^{\rm tot}(\nu_\alpha)$, and $\boldsymbol{p}$ is the vector of model parameters. In our model, the signal ensemble average is

$$\langle \boldsymbol{x}_\alpha \rangle = I^y(\nu_\alpha) + I^\mu(\nu_\alpha) + I^{\rm rec}(\nu_\alpha) + I^T(\nu_\alpha) + \bar{I}^{\rm CIB}(\nu_\alpha) , \qquad (36)$$

whereas the covariance of the data is given by

$$C_\alpha = \left[\delta \bar{I}^{\rm CIB}(\nu_\alpha) \right]^2 + \left[\delta \bar{I}^{\rm CMB}(\nu_\alpha) \right]^2 + \langle \mathcal{N}^2(\nu_\alpha) \rangle$$

$$= \frac{1}{\Omega_{\rm s}^2} \sum_{\ell \geq 2} |W_\ell B_\ell|^2 \left[C_\ell^{\rm CIB}(\nu_\alpha, \nu_\alpha) + C_\ell^{\rm CMB}(\nu_\alpha, \nu_\alpha) \right] + \delta I_\nu^2 . \quad (37)$$

For an all-sky survey, the covariance is simply $C_\alpha = \delta I_\nu^2$. Furthermore, we ignore dependence on cosmological parameters and assume that the recombination signal is perfectly known, so that we can perform an idealized cross-correlation analysis. The model parameters therefore are $\boldsymbol{p} = (\mu, y, \Delta, A_{\rm s}, M_{\rm eff}, T_{\rm d}, \beta, L_0, A_{\rm r})$, where $A_{\rm r}$ is the amplitude of the recombination signal which we seek to constrain. Our fiducial parameter values are $\mu = 10^{-7}$, $y = 5 \times 10^{-7}$, $\Delta = 5 \times 10^{-4}$ and $A_{\rm s} = 2.2 \times 10^{-9}$, together with CIB parameters $M_{\rm eff} = 4.43 \times 10^{12} \, {\rm M}_\odot \, h^{-1}$, $T_{\rm d} = 26$ K, $\beta = 1.7$ and $L_0 = 4.8 \times 10^{-40}$ W Hz^{-1}.

3.2 Experimental setup

The sensitivity of an ideal instrument is fundamentally limited by the noise of incident photons. This is already the case of the best bolometric detectors. For photon noise-limited detectors, a gain

in sensitivity can only be achieved by collecting more photons through an increase in the number of detectors, collecting area and/or integration time.

For the moment, we assume $\mathcal{N}(\nu)$ does not exhibit frequency correlations and is normally distributed with a variance $\langle \mathcal{N}^2 \rangle = \delta I_\nu^2$ which depends only on the bandwidth $\delta\nu$. The analysis is performed assuming top-hat frequency filters, so that the filter response is 1 if $\nu \in [\nu_\alpha - \delta\nu/2, \nu_\alpha + \delta\nu/2]$ and zero otherwise. Regarding the frequency coverage, it is difficult to sample frequencies less than $\sim$30 GHz from space, for which the wavelength becomes larger than the typical size of the device (the collecting area) developed to measure them. However, this frequency regime can be targeted from the ground (see Sathyanarayana Rao et al. 2015, for a recent analysis). Finally, the spectral resolution will be $\delta\nu = 15$ GHz for the PIXIE experiment, but it could be as high as 1 GHz for a satellite mission like MILLIMETRON. For the sake of comparison, we will also consider a ground-based C II mapping instrument which achieve sub-Gigahertz resolution and targets $\mathcal{O}(100)$ GHz frequencies corresponding to C II fine structure lines. We refer the reader to Sathyanarayana Rao et al. 2015 for ground-based surveys probing the $\lesssim 1$ GHz frequency range. Table 1 summarizes the sensitivities of the various setups we consider in our Fisher forecast. Note that the lowest frequency measured is 30 GHz.

We estimate the sensitivity of the ground-based experiment from the requirements given in Gong et al. 2012. Specifically, we consider a single-dish experiment with aperture diameter $D = 10$ m. At 238 GHz (which corresponds to C II emission line at redshift $z = 7$ through the transition $^2P_{3/2} \to {}^2P_{1/2}$; see Gong et al. 2012), the resulting beam FWHM is approximately $\vartheta_{\rm B} = 1.22\lambda/D \approx 0.53$ arcmin. The equivalent beam area is $\Omega_{\rm B} \approx 8.82 \times 10^{-5}$ deg^2. Assuming a noise equivalent flux density of NEFD=10 mJy s$^{1/2}$ per spectral resolution element $\delta\nu = 0.4$ GHz (consistent with the parameters in Gong et al. 2012), we can estimate the sensitivity from the relation

$$\delta I_\nu = \frac{\rm NEFD}{\sqrt{2\tau}\Omega_{\rm B}} , \qquad (38)$$

where τ is the total integration time and the factor of $\sqrt{2}$ arises from the Nyquist sampling and from the assumption of optical chopping.[5] For a total integration time of 4000 h, we find $\delta I_\nu = 50$ Jy sr^{-1} for a single detector. Averaging over 20 000 bolometers, we eventually obtain $\delta I_\nu = 0.35$ Jy sr^{-1}.

Let us assume that the frequency range is evenly split into frequency channels of spectral resolution $\delta\nu_0$, and let δI_0 be the channel sensitivity that can be achieved at this resolution. Since the recombination spectrum features emission lines with a characteristic width of the order of their peak frequency (see Fig. 3), we expect that the signal-to-noise ratio (SNR) for a detection of the recombination spectrum saturates below a certain spectral resolution. This, however, will be true only if the detector follows the standard square-root law SNR $\propto N_\nu^{-1/2}$, where N_ν is the number of frequency channels corresponding to a spectral resolution $\delta\nu$. For a Fourier transform spectrometer (FTS), as utilized in PIXIE and PRISM, the scaling turns out to be SNR $\propto N_\nu^{-1}$.

To see this, we follow Kogut et al. 2011 and consider a total integration time τ. If $N_{\rm s}$ is the number of time-ordered samples used for the Fourier transform, then each sample is observed during

---

[5] The source is measured one-half of the time, and one must differentiate the input signals.

Table 1. Experimental setups considered for the Fisher matrix forecast. The sensitivity of the ground-based experiment was derived for a 10 m aperture telescope at frequency 238 GHz (see the text for details).

	Ω_s	ϑ_B	δI_ν (Jy sr^{-1})	$\delta\nu$ (GHz)	ν-coverage (GHz)
PIXIE	full sky	1°6	5	15	30–600
PRISM	full sky	1°6	0.5	15	30–600
MILLIMETRON	full sky	3 arcmin	10^{-3}	1	100–1000
GROUND C II	16 deg^2	0.5 arcmin	0.35	0.4	185–310

a time τ/N_s. Therefore, the noise in each time-ordered sample of the sky signal $S(t_i)$ is

$$\delta S(t_i) = \frac{\text{NEP}}{\sqrt{\tau/2N_s}} , \qquad (39)$$

where the factor of 2 converts between time and frequency domains (the number of frequency channels is $N_\nu = N_s/2$) and NEP is the noise equivalent power of the detected radiation. Note that NEP generally is a function of frequency. If the noise from different time measurement t_i is uncorrelated, then in each frequency bin of the FTS it is

$$\delta S(\nu_\alpha) = \frac{\delta S(t_i)}{\sqrt{N_\nu}} = \frac{2\text{NEP}}{\sqrt{\tau}} , \qquad (40)$$

independent of the spectral resolution $\delta\nu$ (at fixed $N_\nu\delta\nu$). Therefore, since the sensitivity is $\delta I_\nu(\nu_\alpha) \propto \delta S(\nu_\alpha)/\delta\nu$, we obtain the scaling $\delta I_\nu \propto \delta\nu^{-1} \propto N_\nu$. This implies that the signal-to-noise behaves like SNR $\propto \delta I_\nu^{-1} \propto N_\nu^{-1}$. This also means that (even under idealized conditions) averaging the SNR of individual synthesized FTS channels (improvement of $\simeq \sqrt{N_\nu}$) does not regain you the same sensitivity as directly measuring at lower frequency resolution.

In the FTS case, we thus expect the SNR to reach a maximum at some optimal spectral resolution before falling again as $\delta\nu$ further decreases. Namely, under a change $\delta\nu_0 \rightarrow \delta\nu$ in spectral resolution, the sensitivity of the detector becomes

$$\delta I_\nu = \delta I_0 \left(\frac{\delta\nu_0}{\delta\nu}\right)^\beta = \delta I_0 \left(\frac{N_\nu}{N_0}\right)^\beta , \qquad (41)$$

where $N_\nu\delta_\nu = N_0\delta\nu_0$, while the signal to noise for, say, the model parameter p_i scales like

$$(\text{SNR})^2 = \frac{1}{\delta I_0^2} \left(\frac{N_0}{N_\nu}\right)^{2\beta} \sum_{\alpha=1}^{N_\nu} \left(\frac{\partial I}{\partial p_i}(\nu_\alpha)\right)^2 . \qquad (42)$$

Here, $\beta = 1/2$ and 1 for a square-root law and Fourier transform detector, respectively. Furthermore, we have assumed that both detectors yield the same SNR at the spectral resolution $\delta\nu_0$.

Fig. 4 shows the SNR of the recombination spectrum as a function of spectral resolution for an all-sky satellite experiment that measures the intensity monopole, equation (35), with a sensitivity $\delta I_\nu = 5$ Jy sr^{-1} at spectral resolution $\delta\nu = 15$ GHz, very close to the PIXIE specifications. We consider two different frequency ranges extending up either to 600 GHz or 3 THz, so that the Lyman-α (Ly α) line is only included in the latter case. The other components of our model (see equation 35) have all been marginalized over. Consider a standard square-root detector and measurements in the range $30 < \nu < 600$ GHz for instance. In this case, the SNR decreases mildly as the spectral resolution increases from 10 to 120 GHz, and the Brackett-α (B α) line is gradually smoothed out. The SNR drops abruptly around $\delta\nu \gtrsim 120$ GHz, which corresponds to the disappearance of the Paschen-α (P α) line. Therefore, one
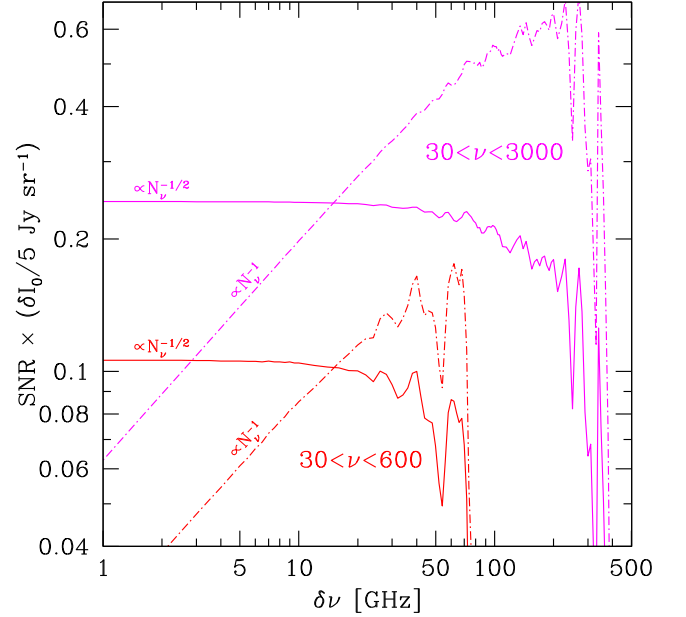

Figure 4. SNR for the detection of the recombination spectrum as a function of spectral resolution after marginalization over the remaining model parameters. We consider two different frequency coverage, $30 < \nu < 600$ and $30 < \nu < 3000$ GHz; as well as two different scaling with the number of frequency channels: $\propto N_\nu^{-1/2}$ (standard square-root law detectors) and $\propto N_\nu^{-1}$ (Fourier transform detectors). The SNR was normalized such that the two different types of detectors yield the same SNR for $\delta\nu = 15$ GHz.

is basically left with only one line, the Balmer-α (H α), at spectral resolution $\delta\nu \gtrsim 120$ GHz unless one extends the measurements out to $\simeq 3$ THz to include the Ly α line (this is quite apparent in Fig. 5). In both cases, the SNR saturates for $\delta\nu \lesssim 10$ GHz for a standard square-root detector whereas, for an FTS, the largest SNR is obtained for $\delta\nu \sim 50$ and ~ 200 GHz. Note that the spectral resolution of PIXIE is 15 GHz, which is close to optimal for a standard square-root detector when the Ly α line is not measured.

3.3 Mitigating the CIB contamination

In order to assess the extent to which the CIB degrades the SNR of the recombination spectrum, consider a PIXIE experiment with sensitivity $\delta I_\nu = 5$ Jy sr^{-1}, spectral resolution $\delta\nu = 15$ GHz and frequency range $30 < \nu < 600$ GHz. Assuming we have perfect knowledge of all the model parameters except the amplitude of the recombination signal, the SNR for the recombination spectrum is SNR $\simeq 0.44$. On marginalizing over the four parameters ($M_{\text{eff}}, T_d, \beta, L_0$) describing the CIB, the SNR drops to 0.17. Further marginalization over the primordial CMB spectral distortions y and μ brings the SNR down to 0.10. For the wider frequency coverage $30 < \nu < 3000$ GHz, the
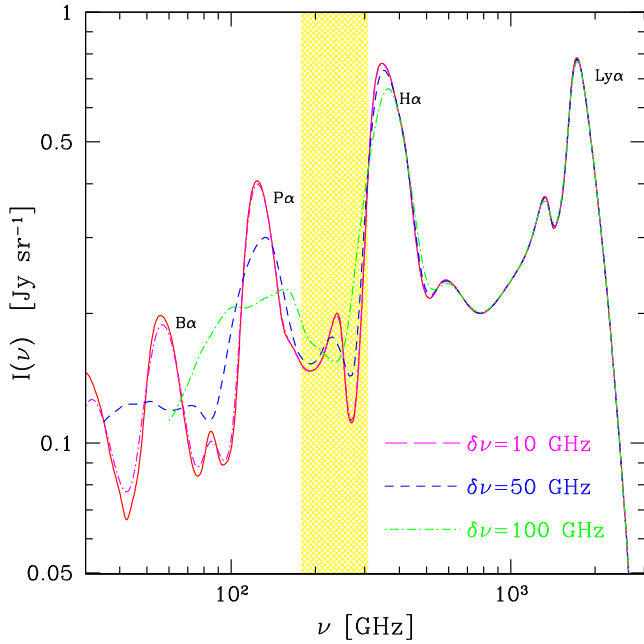
Figure 5. Effect of spectral resolution on the recombination spectrum. At spectral resolution $\delta\nu \gtrsim 100\,\text{GHz}$, the Paschen-$\alpha$ line is wiped out and, unless the frequency coverage is wide enough to include the Ly α line, the SNR drops sharply (see Fig. 4). The shaded region indicates the frequency range probed by the ground C II experiment. In this spectral region, the narrow feature at $\nu \approx 270\,\text{GHz}$ is the combination of two lines with positive and negative peak intensity imprinted during He II$\rightarrow$He I recombination (see Rubiño-Martín et al. 2008).

degradation in the SNR following marginalization over the CIB is nearly a factor of 4 (down from 0.96 to 0.26). Unsurprisingly, the amplitude of the recombination spectrum A_r strongly correlates with M_{eff}, β and L_0 (with a correlation coefficient $|r| \approx 0.9$ in all cases). This is another justification for treating β as free parameter. This also highlights that the continuum part of the cosmological recombination radiation is more difficult to isolate, even if its amplitude may be close to the sensitivity. Accessing the variable component with its quasi-periodic features strongly improves the situation. For an experiment like PRISM, the recombination spectrum could be detected with an SNR of $\simeq 2.4$ if the frequency coverage extends up to 3 THz. Finally, for the MILLIMETRON experiment, the SNR is as large as $\simeq 2500$ for the parameter values quoted in Table 1.

To ascertain the extent to which our CIB model parameters could be constrained by a measurement of the CIB anisotropies, we consider the Fisher matrix (e.g. Pénin et al. 2012)

$$F_{ij}^{\text{CIB}} = \frac{f_{\text{sky}}}{2} \sum_\ell (2\ell + 1) \text{tr}\left[\boldsymbol{C}_\ell^{-1} \frac{\partial \boldsymbol{C}_\ell}{\partial p_i} \boldsymbol{C}_\ell^{-1} \frac{\partial \boldsymbol{C}_\ell}{\partial p_j} \right] . \quad (43)$$

Here, $\boldsymbol{C}_\ell$ is the full, $N_\nu \times N_\nu$ covariance matrix at a given multipole ℓ. The multiplicative factor of f_{sky} reflects the fact that, for partial sky coverage, modes with a given multipole are partially correlated, hence the variance of each measured C_ℓ is larger. The matrix $\boldsymbol{C}_\ell$ takes the form

$$\boldsymbol{C}_\ell = \begin{pmatrix} C_\ell^{\nu_1\nu_1} + \mathcal{N}_\ell^{\nu_1} & C_\ell^{\nu_1\nu_2} & \\ C_\ell^{\nu_2\nu_1} & C_\ell^{\nu_2\nu_2} + \mathcal{N}_\ell^{\nu_2} & \\ & & \ddots \end{pmatrix} , \quad (44)$$

where, for shorthand convenience, $C_\ell^{\nu_i\nu_j} \equiv C_\ell^{\text{CIB}}(\nu_i, \nu_j)$ and $\mathcal{N}_\ell^\nu \equiv \mathcal{N}_\ell(\nu)$ is the angular power spectrum of the instrumental noise. As-
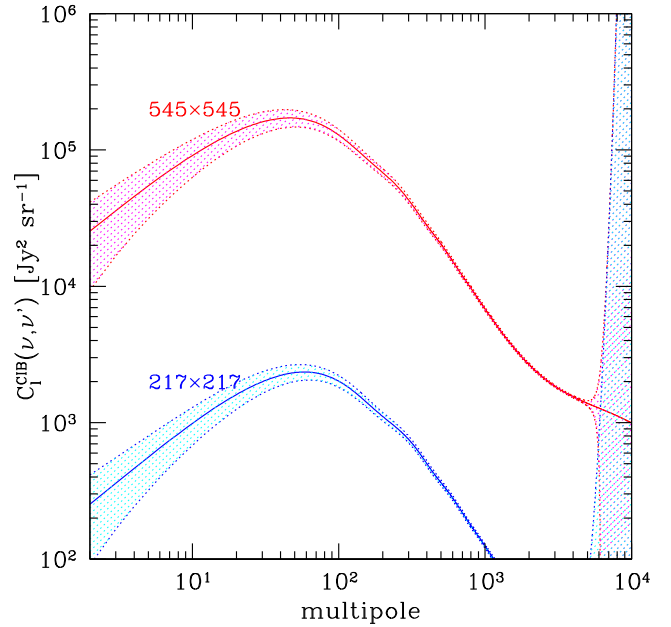

Figure 6. CIB angular power spectrum as measured by an experiment with PRISM sensitivity and a beam angular resolution of 3 arcmin. For the spectral resolution considered, 38×38 cross-power spectra $C_\ell^{\nu\nu'}$ can be computed at each multipole. Notice the flattening at $\ell \gtrsim 1000$ caused by the 1-halo term.

suming uncorrelated and isotropic pixel noise, the latter is given by $\Omega_{\text{pix}}\sigma_{\text{pix}}^2 B_\ell^{-2} \equiv f_{\text{sky}}\omega^{-1}B_\ell^{-2}$ (Knox 1995), where Ω_{pix} is the solid angle subtended by one pixel, σ_{pix} is the noise per pixel and B_ℓ is the experimental beam profile, equation (20). Since our convention is to express the brightness $I(\nu)$ in unit of Jy sr^{-1}, the CIB angular power spectra $C_\ell^{\nu_1\nu_2}$ are in unit of Jy^2 sr^{-1}. The noise per pixel squared is $N_{\text{pix}}\delta I_\nu^2$ whereas the pixel solid angle is $4\pi/N_{\text{pix}}$. Therefore, the weight ω^{-1} is simply $\omega^{-1} = 4\pi\delta I_\nu^2$ and, as expected, is independent of the sky pixelization. For the PIXIE- and PRISM-like specifications, we find $\omega^{-1} = 314$ and 3.14 Jy^2 sr^{-1}, respectively. For illustration, Fig. 6 shows the CIB angular power spectrum at two different frequencies for a PRISM-like experiment with 3 arcmin angular resolution of the imager.

We have evaluated the Fisher matrix equation (43) for these experimental setups with a conservative value of $f_{\text{sky}} = 0.8$, and subsequently computed the SNR for the recombination spectrum upon adding the Fisher information, $F_{ij} = F_{ij}^{\text{mon}} + F_{ij}^{\text{cib}}$, where F_{ij}^{mon} is the Fisher matrix for a measurement of the intensity monopole. For our fiducial beam FWHM of 1°.6 (with $l_{\text{max}} = 1000$), the improvement is negligible. A measurement of the CIB anisotropies at a much finer angular resolution of 3 arcmin (for which we adopt $l_{\text{max}} = 10^4$) somewhat increases the SNR, but the improvement remains small. Namely, for the PIXIE and PRISM-like experiments, respectively, the SNR for a measurement of the recombination spectrum increases from 0.10 to 0.16 and from 1.02 to 1.15 when the angular resolution is changed from 1°.6 to 3 arcmin. This highlights that, in terms of the recombination signal, increased angular resolution is not a main issue. We have not pushed the angular resolution below 3 arcmin as our model does not include shot noise, which we expect to contribute significantly to the $C_\ell^{\nu\nu}$ at multipoles $\ell \gtrsim 10^4$.

We have not computed F_{ij}^{cib} for the small field C II survey because the numerical evaluation is very time-consuming, owing to the exquisite frequency resolution. Nevertheless, Fig. 3 clearly shows that, since patch-to-patch fluctuations in the CIB are a few

orders of magnitude larger than the recombination signal at frequencies $\sim$200 GHz, removing the CIB is an even greater challenge for ground-based surveys targeting those frequencies. In the idealized situation where the CIB is perfectly known and the patch has been cleaned from CMB anisotropies, the SNR is $\simeq 2.74$. The feature at $\nu \approx 270$ GHz (see Fig. 5) helps distinguish the recombination spectrum from the CMB spectral distortions. Overall, our Fisher analysis shows that an all-sky survey covering a large frequency range at moderate frequency resolution $\Delta\nu \sim 10$ GHz will perform much better than an experiment targeting a small patch of the sky at high spectral resolution ($\Delta\nu \sim 0.1$ GHz).

4 CONCLUSIONS

We have presented a Fisher matrix forecast for the detection of the recombination line spectrum with future space experiments. The main caveat of our analysis is the assumption that galactic synchrotron and dust emission have been separated out using low- and high-frequency channels. We have also assumed that most of the thermal SZ effect generated by the LSS can be removed using external catalogues of galaxy clusters when it contributes significantly to the signal covariance (when $f_{sky} \ll 1$). Aside from that, our main findings can be summarized as follows.

(i) The CIB is the main contaminant to the recombination signal. Detecting the recombination lines requires subpercent measurement of the CIB spectral shape at frequencies $\nu \lesssim 1$ THz. The T, y and μ distortions only weakly correlate with the recombination spectrum if the frequency coverage is large enough.

(ii) Adding information from the CIB angular power spectrum does not greatly improve the SNR, even at arcmin angular resolution. Note that we have not considered the possibility of cross-correlating the CIB with LSS to better constrain the CIB model parameters.

(iii) While a ground-based C II-like experiment targeting a small patch of the sky cannot beat the CIB fluctuations, even with very high spectral resolution and exquisite sensitivity, an all-sky satellite mission can do this.

(iv) For an all-sky measurement in the frequency range $30 \leq \nu \leq 600$ GHz, a spectral resolution $\delta\nu \lesssim 10$ GHz is optimal at fixed $\delta\nu\delta I_\nu^2$. For a FTS, the optimal spectral resolution is larger ($\delta\nu \simeq 50$ GHz) and dependent on the frequency coverage (see Fig. 4), owing to the noise-scaling $\delta I_\nu \propto \delta\nu^{-1}$.

(v) A future all-sky satellite mission with sensitivity $\delta I_\nu = 0.1$ Jy sr^{-1} and spectral resolution $\delta\nu = 15$ GHz can detect the recombination lines at 5σ for frequency coverage $30 \leq \nu \leq 600$ GHz. If higher frequency channels are included ($30 \leq \nu \leq 3000$ GHz), a sensitivity of $\delta I_\nu \simeq 0.25$ Jy sr^{-1} is needed for a 5σ detection. This is roughly a factor of 20 more sensitive than the current version of PIXIE. Note that, for an FTS spectrometer, only a factor of 10 improvement is required if one adopts a spectral resolution $\delta\nu \simeq 50$ GHz. An experiment with milli-Jansky sensitivity in frequency channels $\delta\nu = 1$ GHz like MILLIMETRON may measure the recombination lines with an SNR of $\simeq 2500$.

A few more comments are in order. First, the CIB fluctuations are produced by fluctuations in the distribution of high-redshift galaxies and, therefore, should correlate strongly with the fluctuations measured in LSS surveys provided the latter are deep enough to resolve stellar masses of order $M_\star \gtrsim 10^{10-11}$ M$_\odot$ h^{-1}. Therefore, it may be possible to remove the CIB substantially if we overlap with a deep LSS survey. Cross-correlation with LSS data could also be used to mitigate the contamination from e.g. C II emission lines, which we have not considered here.

Secondly, a major issue for the detection of the recombination signals, and any of the primordial distortions really, will be the calibration. To separate different frequency dependent components, a calibration down to the level of the sensitivity is required. In this way, different channels can be compared and the frequency-dependent signals can be separated. For the recombination signal, it may be enough to achieve sufficient channel cross-calibration, since in contrast to the primordial μ and y distortion the signal is quite variable. This issue will have to be addressed in the future.

Finally, we highlight that a detection of the recombination signal also guarantees a detection of the low-redshift y distortion and the small-scale dissipation signals with high significance. These two signals are expected in the standard cosmological model and allow us to address interesting questions about the reionization and structure formation process, as well as the early Universe and inflation physics. Even with a sensitive low-resolution CMB spectrometer it may furthermore be possible to transfer some of the absolute calibration to an independent high-resolution CMB imager like Planck or some future version of PRISM or CORE+. This could further open a possibility to extract the line-scattering signals from the dark ages and the recombination era (Takahara & Sasaki 1991; Yu et al. 2001; Zaldarriaga & Loeb 2002; Basu, Hernández-Monteagudo & Sunyaev 2004; Rubiño-Martín, Hernández-Monteagudo & Sunyaev 2005; Lewis 2013), which in terms of sensitivity are also within reach.

In summary, detection of the hydrogen and helium lines from recombination of the early universe is a hugely challenging but highly rewarding goal for the future of CMB astronomy. This field, largely neglected for three decades, is ripe for exploitation. An all-sky experiment is required to measure the recombination lines. This can best be done from space, or possibly via long duration balloon flights. Likely rewards would include the first spectroscopic study of the very early universe and the first measurement of the primordial helium abundance, as well as unsurpassed probes of new physics and astrophysics in a an entirely new window on the earliest epochs that we can ever directly access by astronomical probes.

REFERENCES

Ali-Haïmoud Y., 2013, Phys. Rev. D, 87, 023526
Allamandola L. J., Tielens A. G. G. M., Barker J. R., 1985, ApJ, 290, L25
Amblard A., Cooray A., 2007, ApJ, 670, 903
André P. et al., 2014, J. Cosmol. Astropart. Phys., 2, 6
Basu K., Hernández-Monteagudo C., Sunyaev R. A., 2004, A&A, 416, 447
Bennett C. L. et al., 2003, ApJS, 148, 1
Berlind A. A., Weinberg D. H., 2002, ApJ, 575, 587
BICEP2 Collaboration et al., 2014, Phys. Rev. Lett., 112, 241101
Bond J. R., Efstathiou G., 1984, ApJ, 285, L45
Burigana C., Salvaterra R., 2003, MNRAS, 342, 543
Burigana C., Danese L., de Zotti G., 1991, A&A, 246, 49

Cen R., Ostriker J. P., 1999, ApJ, 514, 1
Chluba J., 2013a, MNRAS, 434, 352
Chluba J., 2013b, MNRAS, 436, 2232
Chluba J., Grin D., 2013, MNRAS, 434, 1619
Chluba J., Jeong D., 2014, MNRAS, 438, 2065
Chluba J., Sunyaev R. A., 2004, A&A, 424, 389
Chluba J., Sunyaev R. A., 2006, A&A, 458, L29
Chluba J., Sunyaev R. A., 2008, A&A, 478, L27
Chluba J., Sunyaev R. A., 2010, MNRAS, 402, 1221
Chluba J., Sunyaev R. A., 2012, MNRAS, 419, 1294
Chluba J., Rubiño-Martín J. A., Sunyaev R. A., 2007, MNRAS, 374, 1310
Chluba J., Vasil G. M., Dursi L. J., 2010, MNRAS, 407, 599
Chluba J., Khatri R., Sunyaev R. A., 2012a, MNRAS, 425, 1129
Chluba J., Erickcek A. L., Ben-Dayan I., 2012b, ApJ, 758, 76
Clesse S., Garbrecht B., Zhu Y., 2014, J. Cosmol. Astropart. Phys., 10, 46
Crill B. P. et al., 2008, in Oschmann J. M., Jr. de Graauw M. W. M., MacEwen H. A., eds, Proc. SPIE Conf. Ser. Vol. 7010, Space Telescopes and Instrumentation 2008: Optical, Infrared, and Millimeter. SPIE, Bellingham, p. 70102P
Daly R. A., 1991, ApJ, 371, 14
Danese L., de Zotti G., 1982, A&A, 107, 39
De Bernardis F., Cooray A., 2012, ApJ, 760, 14
Dent J. B., Easson D. A., Tashiro H., 2012, Phys. Rev. D, 86, 023514
Dubrovich V. K., 1975, Sov. Astron. Lett., 1, 196
Dubrovich V. K., Stolyarov V. A., 1995, A&A, 302, 635
Dubrovich V. K., Stolyarov V. A., 1997, Astron. Lett., 23, 565
Eimer J. R. et al., 2012, in Holland W. S., Zmuidzinas J., eds, Proc. SPIE Conf. Ser. Vol. 8452, Millimeter, Submillimeter, and Far-Infrared Detectors and Instrumentation for Astronomy VI. SPIE, Bellingham, p. 845220
Emami R., Dimastrogiovanni E., Chluba J., Kamionkowski M., 2015, preprint (arXiv:1504.00675)
Fixsen D. J., 2009, ApJ, 707, 916
Fixsen D. J., Cheng E. S., Gales J. M., Mather J. C., Shafer R. A., Wright E. L., 1996, ApJ, 473, 576
Ganc J., Komatsu E., 2012, Phys. Rev. D, 86, 023518
Gong Y., Cooray A., Silva M., Santos M. G., Bock J., Bradford C. M., Zemcov M., 2012, ApJ, 745, 49
Guo Q., White S., Li C., Boylan-Kolchin M., 2010, MNRAS, 404, 1111
Hall N. R. et al., 2010, ApJ, 718, 632
Hu W., Silk J., 1993, Phys. Rev. D, 48, 485
Hu W., Sugiyama N., 1994, ApJ, 436, 456
Hu W., Scott D., Silk J., 1994a, Phys. Rev. D, 49, 648
Hu W., Scott D., Silk J., 1994b, ApJ, 430, L5
Illarionov A. F., Sunyaev R. A., 1975, Sov. Astron., 18, 413
Kamionkowski M., Kosowsky A., 1998, Phys. Rev. D, 57, 685
Kamionkowski M., Kosowsky A., Stebbins A., 1997, Phys. Rev. D, 55, 7368
Khatri R., Sunyaev R. A., 2012, J. Cosmol. Astropart. Phys., 9, 16
Khatri R., Sunyaev R. A., 2013, J. Cosmol. Astropart. Phys., 6, 26
Knox L., 1995, Phys. Rev. D, 52, 4307
Knox L., Cooray A., Eisenstein D., Haiman Z., 2001, ApJ, 550, 7
Kogut A. et al., 2011, J. Cosmol. Astropart. Phys., 7, 25
Komatsu E., Kitayama T., 1999, ApJ, 526, L1
Kravtsov A. V., Berlind A. A., Wechsler R. H., Klypin A. A., Gottlöber S., Allgood B., Primack J. R., 2004, ApJ, 609, 35
Leger A., Puget J. L., 1984, A&A, 137, L5
Lewis A., 2013, J. Cosmol. Astropart. Phys., 8, 53
Lewis A., Challinor A., Lasenby A., 2000, ApJ, 538, 473
Limber D. N., 1954, ApJ, 119, 655

McDonald P., Scherrer R. J., Walker T. P., 2001, Phys. Rev. D, 63, 023001
Manzotti A., Hu W., Benoit-Lévy A., 2014, Phys. Rev. D, 90, 023003
Miniati F., Ryu D., Kang H., Jones T. W., Cen R., Ostriker J. P., 2000, ApJ, 542, 608
Pajer E., Zaldarriaga M., 2012, Phys. Rev. Lett., 109, 021302
Pajer E., Zaldarriaga M., 2013, J. Cosmol. Astropart. Phys., 2, 36
Pénin A., Doré O., Lagache G., Béthermin M., 2012, A&A, 537, A137
Persi F. M., Spergel D. N., Cen R., Ostriker J. P., 1995, ApJ, 442, 1
Planck Collaboration XVI, 2014a, A&A, 571, A16
Planck Collaboration XXX, 2014b, A&A, 571, A30
Planck Collaboration XVII 2015a, preprint (arXiv:1502.01592)
Planck Collaboration XIII 2015b, preprint (arXiv:1502.01589)
Powell B. A., 2012, preprint (arXiv:1209.2024)
Refregier A., Komatsu E., Spergel D. N., Pen U.-L., 2000, Phys. Rev. D, 61, 123001
Rubiño-Martín J. A., Hernández-Monteagudo C., Sunyaev R. A., 2005, A&A, 438, 461
Rubiño-Martín J. A., Chluba J., Sunyaev R. A., 2006, MNRAS, 371, 1939
Rubiño-Martín J. A., Chluba J., Sunyaev R. A., 2008, A&A, 485, 377
Rybicki G. B., dell'Antonio I. P., 1993, in Chincarini G. L., Iovino A., Maccacaro T., Maccagni D., eds, ASP Conf. Ser. Vol. 51, Observational Cosmology. Astron. Soc. Pac., San Francisco, p. 548
Sathyanarayana Rao M., Subrahmanyan R., Udaya Shankar N., Chluba J., 2015, preprint (arXiv:1501.07191)
Seljak U., Zaldarriaga M., 1997, Phys. Rev. Lett., 78, 2054
Serra P., Lagache G., Doré O., Pullen A., White M., 2014, A&A, 570, A98
Shang C., Haiman Z., Knox L., Oh S. P., 2012, MNRAS, 421, 2832
Silk J., Chluba J., 2014, Science, 344, 586
Silk J., Wilson M. L., 1980, Phys. Scr., 21, 708
Smirnov A. V. et al., 2012, in Clampin M. C., Fazio G. G., MacEwen H. A., Oschmann J. M., Jr, eds, Proc. SPIE Conf. Ser. Vol. 8442, Space Telescopes and Instrumentation 2012: Optical, Infrared, and Millimeter Wave. SPIE, Bellingham, p. 84424C
Smith J. D. T. et al., 2007, ApJ, 656, 770
Staniszewski Z. et al., 2012, J. Low Temp. Phys., 167, 827
Stebbins A., 2007, preprint (astro-ph/0703541)
Sunyaev R. A., Chluba J., 2009, Astron. Nachr., 330, 657
Sunyaev R. A., Zeldovich Y. B., 1970a, Ap&SS, 7, 3
Sunyaev R. A., Zeldovich Y. B., 1970b, Ap&SS, 7, 20
Sunyaev R. A., Zeldovich Y. B., 1970c, Ap&SS, 9, 368
Takahara F., Sasaki S., 1991, Prog. Theor. Phys., 86, 1021
Tegmark M., Taylor A. N., Heavens A. F., 1997, ApJ, 480, 22
Tinker J. L., Wetzel A. R., 2010, ApJ, 719, 88
Tinker J., Kravtsov A. V., Klypin A., Abazajian K., Warren M., Yepes G., Gottlöber S., Holz D. E., 2008, ApJ, 688, 709
Tinker J. L., Robertson B. E., Kravtsov A. V., Klypin A., Warren M. S., Yepes G., Gottlöber S., 2010, ApJ, 724, 878
White M., Srednicki M., 1995, ApJ, 443, 6
Yu Q., Spergel D. N., Ostriker J. P., 2001, ApJ, 558, 23
Zaldarriaga M., Loeb A., 2002, ApJ, 564, 52
Zehavi I. et al., 2011, ApJ, 736, 59
Zeldovich Y. B., Sunyaev R. A., 1969, Ap&SS, 4, 301
Zeldovich Y. B., Illarionov A. F., Sunyaev R. A., 1972, Sov. J. Exp. Theor. Phys., 35, 643
Zhang P., Pen U.-L., Trac H., 2004, MNRAS, 355, 451
Zheng Z. et al., 2005, ApJ, 633, 791

This paper has been typeset from a TeX/LaTeX file prepared by the author.